CrossMark

Effect of heat input in pulsed Nd:YAG laser welding of titanium alloy (Ti6Al4V) on microstructure and mechanical properties

Pramod Kumar[1] · Amar Nath Sinha[1]

Abstract

In the present investigation, titanium alloy Ti6Al4V of 1.4 mm thickness has been laser-welded in butt joint configuration using pulsed Nd:YAG laser system. The effects of heat input on weld bead shape, fusion zone width (top, middle, and bottom), heat-affected zone (HAZ) width (top, middle, and bottom), and fusion zone area have been studied. The microstructure and mechanical properties of laser-welded specimens at various heat inputs (43.7–103.5 J/mm) have also been investigated. Microstructures of the fusion zone, HAZ, and parent material have been compared at various heat inputs using optical microscope and field emission scanning electron microscope (FESEM). The mechanical properties such as microhardness and tensile strength of the welded joints at varying heat inputs have been studied. Tensile tests of the welded specimen and base metal have been conducted for analyzing ultimate tensile strength and percentage elongation. Surface topography of the tensile fractured specimen of the welded joints and base metal has been examined to analyze the ductile and brittle behavior. EDS analyses of base metal and fusion zone of the welded specimen have been studied. XRD of the as-received base metal and welded specimen have been measured in the range of 30 to 85° to study the crystallographic structure.

Keywords Laser beam welding · Ti6Al4V · Microhardness · Pulsed Nd:YAG laser · Porosity · Microstructure

1 Introduction

Ti6Al4V has wide applications in nuclear, aerospace, automobile, medical, and petrochemical industries due its high corrosion resistance, high strength, low density, and creep resistance [1]. Titanium alloys are bio-compatible as they are widely used for bio-medical applications like artificial heart pumps, pacemaker cases, and heart valve parts [2]. Titanium and its alloys are commonly welded using many joining processes such as gas tungsten arc welding (GTAW), metal arc welding (MAW), electron beam welding (EBW), laser beam welding (LBW), and friction stir welding [3, 4]. LBW is widely used, compared to other welding processes due to its high flexibility, high precision, spatter free welds, lower distortion,

and narrower heat-affected zone [5]. Ti6Al4V and its alloys act as bridge between the properties of steel and aluminum. Titanium alloys have two crystallographic forms, namely, α-titanium having hcp crystal lattice and β-titanium having bcc crystal lattice. Pure titanium exists in a form of α-phase at temperatures above 883 °C and in a form of β-phase at temperatures below 883 °C. The temperature of allotropic transformation of α-titanium to β-titanium is called beta transus temperature. Alloying elements in titanium alloys may stabilize either α-phase or β-phase of the alloy. Al, Ga, N, and O stabilize α-phase whereas Mo, V, W, Ta, and Si stabilize β-phase. Titanium alloys are used in place of aluminum-based materials when operating temperature is more than 130 °C to achieve better mechanical properties at high temperature, as applicable in turbine blades, landing gear, and structural components used in Boeing 747 [6]. Titanium alloys have low thermal conductivity (22 W cm^{-1} K^{-1}) which prevents heat dissipation and low thermal expansion coefficient which avoids the appearance of stresses during welding. Titanium alloys have low heat input, which reduces the stresses developed and distortion produced. Titanium alloys show a good rate of laser beam absorption (0.4%) and high melting point (1670 °C) [7, 8]. The abovementioned properties of titanium

✉ Pramod Kumar
pramod.me14@nitp.ac.in

[1] Department of Mechanical Engineering, National Institute of Technology Patna, Ashok Rajpath, Patna 800005, India

⚫ Springer

alloys imply that high energy must be used to join these alloys. Therefore, laser beam welding is an adequate technology to join these alloys as it allows a high localization and low size of the melt pool, reducing the required energy considerably in comparison with other joining processes.

LBW is a nonconventional and advanced joining process for similar or dissimilar materials. Laser welding is widely used for welding commercially pure titanium and many of titanium alloys. Titanium alloys are highly reactive with atmosphere at elevated temperature; therefore, additional shielding of the weld pool must be provided which can be done by LBW as it forms the keyhole which effectively concentrates the heat input into the weld pool resulting into narrow heat-affected zone (HAZ) and better mechanical property [9]. There are basically three different modes of laser welding, namely, conduction mode, mixed mode, and keyhole mode. In conduction mode, the absorbed laser energy heats the material to melting temperature keeping the surface temperature between the melting and boiling points and weld penetration is achieved by the laser heat conducting down into the metal from the surface. When the temperature exceeds the boiling point, evaporation will occur at the laser front and the material removal creates a keyhole in the workpiece whereas when the keyhole does not extend to the melt front, the weld so formed is named as mixed mode [10]. In keyhole mode, the power density is great enough to vaporize the metal which expands the gas and pushes outward creating a keyhole or tunnel from surface to the weld depth [11]. The amount of heat energy developed during LBW is more compared to other conventional welding processes. The weld pool formed in the laser welding is too smaller compared to that in the arc welding process. LBW forms superior quality of titanium alloy weld comparative to EBW. LBW is a highly automated joining process with production rates higher than those for EBW. LBW are not restricted by component size as Nd:YAG laser delivery systems can be used, allowing the welding head to be remote from the power source whereas component size is restricted by the size of vacuum chamber in EBW. LBW is a noncontact welding process so magnetic materials can be easily welded whereas EBW requires demagnetizing treatment for steel plates to weld. LBW is also a suitable welding process for joining of dissimilar materials as it is a combined effect of high energy density and greater welding speed which consecutively decreases the thickness of the reactive interlayer and retards the formation of intermetallic phases [12].

Many researchers have investigated the joining of pure titanium and titanium alloys. Torkamany et al. [13] have investigated the pulsed Nd:YAG laser welding of commercially pure titanium. They have observed that with increase in pulse peak power and keyhole formation, spattering and weld porosity increase in the weldment. They have also found that the depth of penetration (DOP) increases at elevated values of pulse energy and pulse duration and constant peak power.

Akman et al. [14] explored the effect of laser process parameters, namely, pulse energy, pulse width, pulse shape, pulse frequency, and pulse peak power on seam weld quality of titanium sheet of 3 mm thickness. They have observed that among the selected laser process parameters, pulse energy and pulse width mostly influence the penetration of the welded joint. They have also found that there is no significant change in DOP with varying pulse duration at constant peak power. Gao et al. [15] have studied the influence of low and high heat input on weld cross-section profiles, microstructure, and mechanical properties of laser welding of titanium alloy (Ti6Al4V) in pulse mode using Nd:YAG laser. They have observed that the V- and H-shaped weld cross-section geometries were formed at low and high heat input, respectively. The tensile strength of H-shaped welded joint was more than that of V-shaped as H-shaped welded joint fractured in the BM while V-shaped welded joint fractured near the HAZ and BM interface. Xu et al. [16] have investigated the slip deformation and microstructure characterization of laser welding of Ti6Al4V titanium alloy. They have observed the presence of slip deformation in fractured and etched welds and were energized by external forces and welding residual stresses developed. They have found that the maximum compression strength of the welded joint was 1.191 GPa. They have also observed that the minimum slip bands occurred in the fractured and etched laser welds were 600 nm and 75 nm, respectively. Gao et al. [17] have explored the influence of the overlapping factor (O_f) in laser welding of titanium alloy of 0.8 mm thickness with pulsed Nd:YAG laser system. They have found that the HAZ width of the welded joint increases and grains of the fusion zone becomes coarser with increase in overlapping factor. They have also found that the welded joints at medium overlapping factor showed better mechanical strength compared to those at low and high overlapping factors. Gursel et al. [18] have studied the presence of cracks in the Ti6Al4V welded joint. They have observed that the Ti6Al4V alloys were satisfactorily welded by Nd:YAG laser compared to other conventional joining processes. They have also observed that optimum results for titanium welded joint were obtained at peak power of 3.9 kW and superior ductility was obtained when grade 1 titanium alloy was used as a filler material. Caiazzo et al. [19] have investigated the laser welding of Ti6Al4V alloy of 3-mm-thick plate for butt-welded corner joint configuration to be applicable in aerospace industries. They have found the optimum laser process parameters for minimum undercut and porosity in the welded joint. Kumar et al. [20] have explored the fiber laser welding of Ti6Al4V alloy of 5 mm thickness using 2-kW fiber laser based on statistical design of experiment in continuous wave mode. They have studied the effect of laser process parameters, namely, scanning speed, beam power, and defocused position on fusion zone width, HAZ width, and fusion zone area. They have observed that the beam power and scanning speed

are the most influencing process parameters for achieving full depth of penetration and also found that the beam power shows the direct effect whereas scanning speed shows the inverse effect with the output responses measured. Campanelli et al. [21] have studied laser welding of Ti6Al4V of 2 mm thickness for butt joint configuration using Fiber Ytterbium laser system of 4 kW. They have investigated the influence of constant laser beam power and varying welding speed on weld characteristics and mechanical properties. They have observed that specific heat input has more effect on weld bead shape. Caiazzo et al. [22] have explored the influence of laser beam power, welding speed, and defocus in laser welding of Ti6Al4V plate of 3 mm thick using a disk laser source in continuous wave. They have observed that the fusion zone of the welded joint consisted of acicular α' martensite and also optimized process parameters for the minimization of fusion zone and mean grain size. The numerical simulations of temperature distribution of LBW of Ti6Al4V for predicting the HAZ, DOP, and the width of molten pool have been investigated by Akbari et al. [23]. They have also validated the numerical results with experimental results with good agreement. They have observed that the peak temperature decreased sharply near the laser beam center and decreased slightly away from the laser beam center. Oliveira et al. [24] have explored the detailed review for joining process of NiTi shape memory alloys. They have studied the weldability problems such as reduced strength, formation of brittle intermetallic, changes in phase transformation, and shape memory effects in NiTi. They have found that NiTi are commonly laser-welded due to low heat input on the base material. Oliveira et al. [25] have also studied the dissimilar laser welding of NiTi and Ti6Al4V using niobium interlayer to restrict the formation of brittle intermetallics in the weldment. They have observed a defect free weld with tensile strength and elongation of the welded joint equal to 300 MPa and 2%, respectively. Auwal et al. [26] have investigated the review on similar and dissimilar laser beam welding of titanium alloys to study the influence of the laser process parameters, microstructure study, weld defects, and possible remedies. Sjögren et al. [27] have investigated the laser welding of titanium for dental application. They have studied the tensile strength, proof stress, and elongation of laser-welded joints at different laser process parameters and also compared the fracture behavior of the laser-welded joints and base metal. The fracture surface of the welded specimens showed various defects, namely, gas pores and cracks, compared to the parent metal. Palanivel et al. [28] have investigated the microstructure and mechanical characterization of Nd:YAG laser welding of titanium tubes of 60 mm outer diameter and 3.9 mm wall thickness. They have observed the presence of spherical and irregular shaped pores near the centerline of the fusion zone due to entrapment of gases from the atmosphere during solidification.

From literature review presented so far, it has been observed that very limited work has been done in the area of pulsed Nd:YAG laser welding of Ti6Al4V, to study the influence of heat input on microstructural characterization and mechanical properties of laser-welded joints using low-power Nd:YAG laser generator. The objective of the present research work is to study the influence of heat input on weld bead shape, fusion zone width (top, middle, and bottom), HAZ width (top, middle, and bottom), and fusion zone area. The microstructural characterization and mechanical properties, namely, microhardness and tensile strength, of the welded specimens and base metal have been investigated.

2 Experimental procedure

In the present study, pulsed Nd:YAG laser of 600-W maximum average power integrated with IRB 1410 robotic control was used. The pictorial view of the experimental setup for Nd:YAG laser system is shown in Fig. 1a. The experimental condition and laser machine specification are given in Table 1.
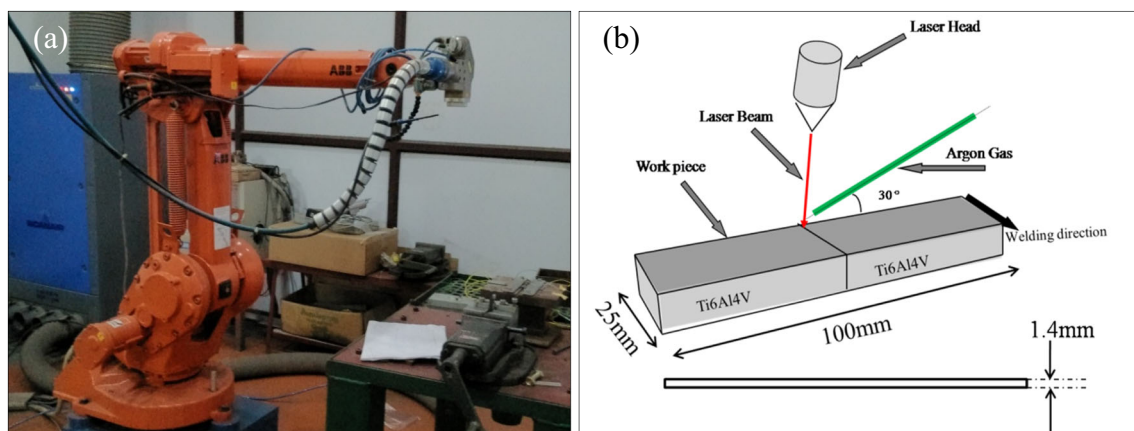

Fig. 1 **a** Pictorial view of the pulsed Nd:YAG laser beam welding setup and **b** schematic diagram of LBW setup showing workpiece dimension and welding direction

Table 1 Experimental condition and machine specification of the laser beam welding

Specification	Value
Laser power mode	Square pulsed wave
Maximum average power at laser (W)	600
Typical power at workpiece (W)	500
Max. peak power (W)	10
Max. pulse energy (J)	100
Max. frequency (Hz)	1000
Pulse width range (ms)	0.2–20
Beam quality (mm mrad)	28
Standard fiber length (m)	5
Max. focal length (mm)	160
Laser spot diameter (mm)	0.45
Type of shielding gas used	Argon (99.9% pure)

The laser head was kept at an angle of 15° with the vertical axis to restrict the reflection of workpiece. Ti6Al4V sheets of 1.4 mm thickness were laser-welded in butt joint configuration at different laser process parameters with varying heat inputs. The workpiece having a dimension of 50 mm × 25 mm × 1.4 mm was clamped on the base plate using a special fixture to reduce the distortion and movement of the specimens during laser welding. The schematic diagram of the LBW setup showing workpiece dimension, welding direction, and argon shielding gas delivery system is shown in Fig. 1b. The chemical composition of the as-received base metal Ti6Al4V of 1.4 mm thickness measured by energy-dispersive X-ray (EDX) analysis is shown in Table 2.

The combination of pulse frequency and pulse energy has been selected in such a way that the average beam power would not exceed 600 W. Argon gas (99.9% pure) with a flow rate of 6 l/min was used as shielding gas. The laser welding process parameters with experimental observations are tabulated in Table 3. The laser beam spot diameter for all experiments was taken as 0.45 mm.

The heat input (HI) and overlapping factor (O_f) given in Table 3 have been evaluated using Eqs. (1) and (2) as given by Gao et al. [17, 29].

$$HI = \left(\frac{P \times T \times f}{V} \right) \times \eta \qquad (1)$$

$$O_f = [1 - (V/f)/(D + VT)] \times 100 \qquad (2)$$

Table 2 The chemical composition of Ti6Al4V (wt%)

Grade	C	N	O	Fe	Al	W	V	Ti
Ti6Al4V	2.33	2.17	4.01	0.23	3.01	0.31	11.19	Bal.

where P is peak power (kW), T is pulse width (ms), f is pulse frequency (Hz), V is scanning speed (mm/s), D is laser spot size (mm), and η is welding efficiency. η has been assumed a constant value equal to 1, as the efficiency remains unchanged for the same material and welding process considered.

The laser-welded specimens were prepared as per ASTM for metallographic examination [30]. Firstly, the transverse section of the welded specimens was cut with wire EDM of dimension 10 mm × 3.75 mm × 1.4 mm and mounted using cold mounting powder and liquid. The specimens were polished using several grades (180–1500 grits) of silicon carbide emery papers and were polished on velvet cloth using abrasives like alumina and colloidal silica of 0.25 and 0.03 μm respectively for getting mirror polished finished surface. The polished specimens were further cleaned in ultrasonic cleaner using acetone. For etching the transverse section of the welded joints, the final polished specimens were immersed into the aqueous solution of Kroll's reagent (92 ml distilled water, 6 ml HNO_3, and 2 ml HF) for 20 s. The schematic diagram of the weld bead geometry is shown in Fig. 2. Microstructural characterization of the welded joint was performed using Leica optical microscope and FESEM. The microstructure of the fusion zone was also characterized using high-resolution transmission electron microscope (TEM). The microhardness of the welded specimens was measured using INNOVA TEST FALCON 500 at constant load of 0.98 N and dwell time of 20 s. The hardness was measured in the middle of the transverse section of the welded specimen with an interval of 0.10 mm starting from weld center of fusion zone to base metal zone on both sides of the weld center. The tensile samples of the base metal and welded specimens were prepared as per the ASTM E8 standards [31] as shown in Fig. 3. The tensile test was carried out on INSTRON 1195 tensile testing machine with 50 kN maximum load and crosshead speed of 2 mm/min.

3 Results and discussion

The laser welding experimental results at different process parameters are briefly discussed in the following subsections.

3.1 Influence of heat input on weld surface appearance

The appearance of the top and bottom surface of the welded samples at different welding parameters is shown in Figs. 4 and 5, respectively. The bead appearance of Ti6Al4V helps in the detection of oxidation and effectiveness of shielding gas as reported by Hong and Shin [32]. It has been observed that as the heat input increases, the weld zone width increases on both top and bottom surfaces. The bottom surface of the weld bead obtained at low heat input of 43.71 J/mm (exp. 1) is not

Table 3 Pulsed Nd:YAG LBW process parameters with overlapping factor and ultimate tensile strength	Sl. no.	Average power (W)	Heat input (J/mm)	Peak power (kW)	Scanning speed (mm/s)	Pulse duration (ms)	Frequency (Hz)	Overlapping factor	UTS (MPa)
	1.	300	43.714	3.272	7	5.5	17	15.708	652.93
	2.	340	48.571	3.4	7	5	20	27.835	686.22
	3.	300	49.98	3.6	6	5	16.66	24.969	820.67
	4.	340	60	3.272	6	5.5	20	37.888	693.03
	5.	380	75.6	3.272	5	5.5	21	50.137	444.05
	6.	420	103.5	3.272	4	5.5	23.33	63.154	340.62

uniform compared to others. All the weld surfaces obtained from LBW as shown in Figs. 4 and 5 are esthetic and dark straw color indicating the optimum shielding effectiveness of the weld pool from the external atmosphere. The appearance of cavities and blow holes can be seen at high heat input of 75.6 and 103.5 J/mm (exp. 5 and 6) due to evaporation of alloying elements having low boiling point, present in Ti6Al4V. Good weld bead appearance has been observed at heat input greater than 43.71 J/mm but smaller than 75.6 J/mm during laser welding of Ti6Al4V, to get minimum weld defects. The spattering effect has also been observed at high heat input of 60, 75, and 103.5 J/mm as shown on the back side of the weld bead zone for exp. nos. 4, 5, and 6 as shown in Fig. 5. Spattering occurs due to high reactivity of Ti6Al4V at high heat input during LBW.

3.2 Influence of heat input on weld bead cross-section profile

Figure 6 shows the weld bead cross-section profile obtained by LBW carried out at different welding conditions given in Table 3. Full depth of penetration was observed for all the laser-welded specimens, obtained at different laser process parameters. There were two different types of weld bead shapes observed, namely, T-shaped and X-shaped, in the present study at different heat inputs ranging from 43.71 to

103.5 J/mm. The shape of the weld bead is nearly T-shaped at heat input of 43.71, 48.57, 49.98, 60, and 75.6 J/mm (exp. 1, 2, 3, 4, and 5) and changes to nearly X-shaped at high heat input of 103.5 J/mm (exp. 6) as shown in Fig. 6.

The vaporization of molten pool takes place during initial phase of keyhole formation in LBW. The behavior of molten metal flow pattern is entirely dependent upon recoil pressure, surface tension, and gravity force, and the recoil pressure developed depends on the intensity of laser beam. Multiple reflections of the laser beam occur inside the keyhole, which generates a temperature difference between the top and bottom surfaces of the melt pool. Surface tension also varies between the two melt pool surfaces due to temperature difference, which creates a recoil pressure along the keyhole leading to enlarge size of the melt pool in lower portion. The top and bottom melt pool areas get expanded due to continuous escaping of the reflected laser beam from upper and lower half of the weld pool and lead to the formation of keyhole open at the root side which is named as open keyhole as shown in Fig. 7a. The solidification of the melt pool in open keyhole mode forms an X-shaped weld bead as shown in Fig. 6f. The reflected laser beam intensity inside the keyhole is lower at low heat input, and lower half of the melt pool is comparatively less expanded as the surface tension developed is canceled by the recoil pressure. Therefore, during solidification of the melt pool, the keyhole remains closed
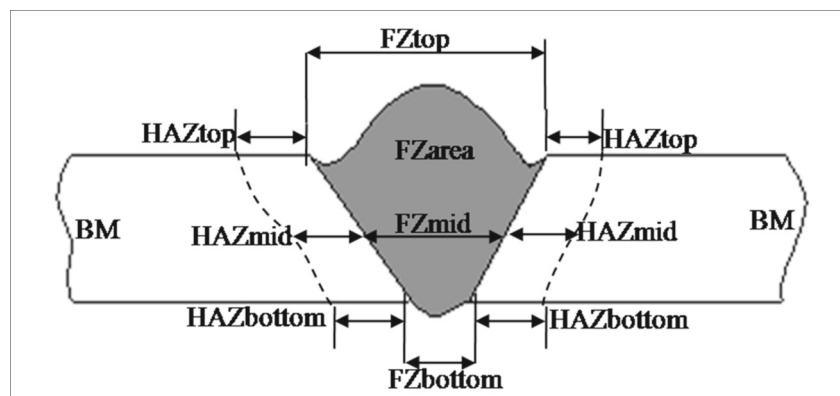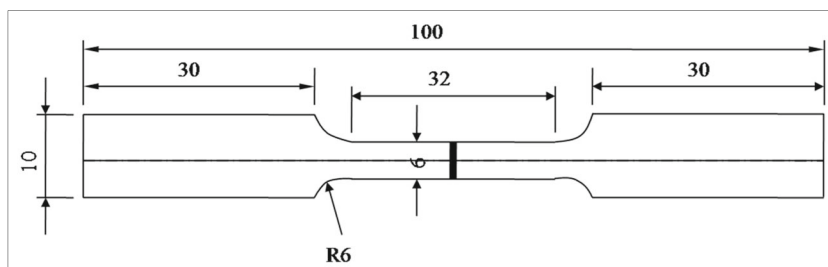

Fig. 2 Schematic diagram of weld bead geometry

slightly at the root and the keyhole so formed is named as closed keyhole as shown in Fig. 7b. The solidification of the melt pool in closed keyhole mode forms the T-shaped weld bead as shown in Fig. 6a–e.

3.3 Influence of heat input on FZ area, HAZ width, and FZ width

Figure 8a, b shows the influence of heat input on fusion zone area and fusion zone width (top, middle, and bottom). The fusion zone area increases linearly with increase in heat input as shown in Fig. 8a. From Fig. 8b, it has been observed that the top weld bead width and bottom weld bead width increase with increase in heat input as the heat energy supplied on the workpiece surface increases with increase in heat input. The increasing trend of FZ width with increasing heat input was also observed by Squillance et al. [33]. The FZ top width is larger than the FZ mid and FZ bottom for all the laser welding experiments performed because the molten metal flows more in the upper portion of the weld pool compared to that in the lower portion of the weld pool which distorts the keyhole shape and producing wider top weld bead width and narrower bottom weld bead width. The effect of heat input on heat-affected zone width (HAZ top, HAZ mid, and HAZ bottom)

is shown in Fig. 8c. The mechanical properties of the laser-welded specimens are greatly influenced by the width of HAZ formed. The HAZ mid and HAZ bottom continuously increase with increase in heat input whereas HAZ top first increases and then becomes constant and again further increases with increase in heat input.

3.4 Microstructure study of HAZ and fusion zone

The microstructural characterization of the fusion zone, HAZ, and base metal has been done in the present section. The microstructure of the base metal Ti6Al4V mainly consists of white equiaxed intergranular β-phase and gray equiaxed globular α-phase as shown in Fig. 9a, b at low and high magnification of FESEM image. The intergranular β-phase present in the base metal is scattered in the matrix of globular α-phase having different grain dimensions.

The change in the concentration (wt%) of alloying constituents of the base metal Ti6Al4V and fusion zone of the welded specimen is characterized by energy-dispersive spectrometer (EDS). Figure 10 shows the EDS analysis of base metal and fusion zone for exp. no. 3.

Laser welding process consists of two steps, i.e., heating stage and cooling stage. The increase in volume fraction of β-
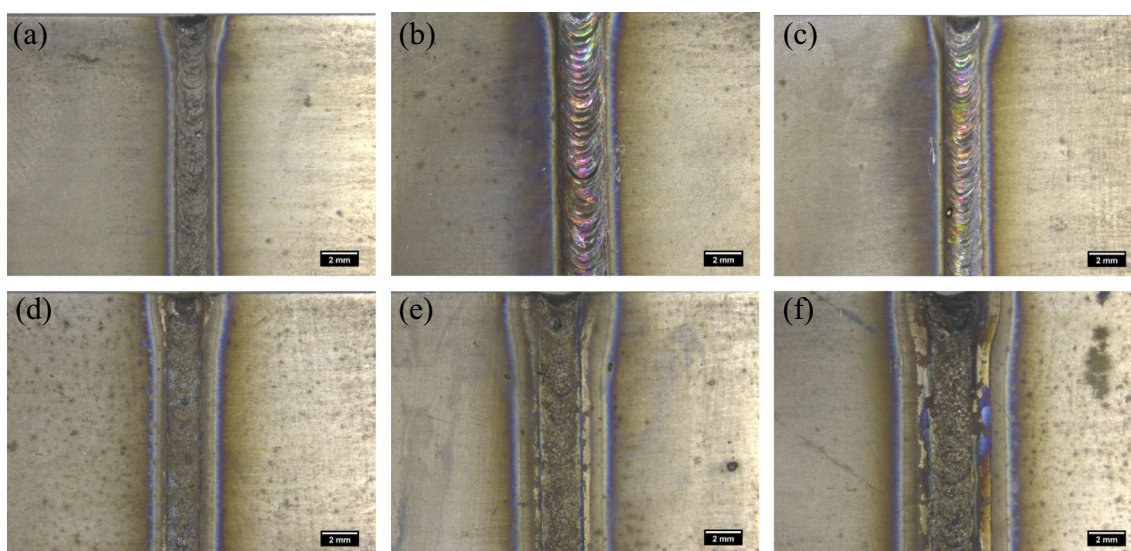

Fig. 4 Weld bead appearance of the top surface of the welded joints at varying heat inputs: **a** 43.71 J/mm, **b** 48.57, **c** 49.98 J/mm, **d** 60 J/mm, **e** 75.6 J/mm, and **f** 103.5 J/mm
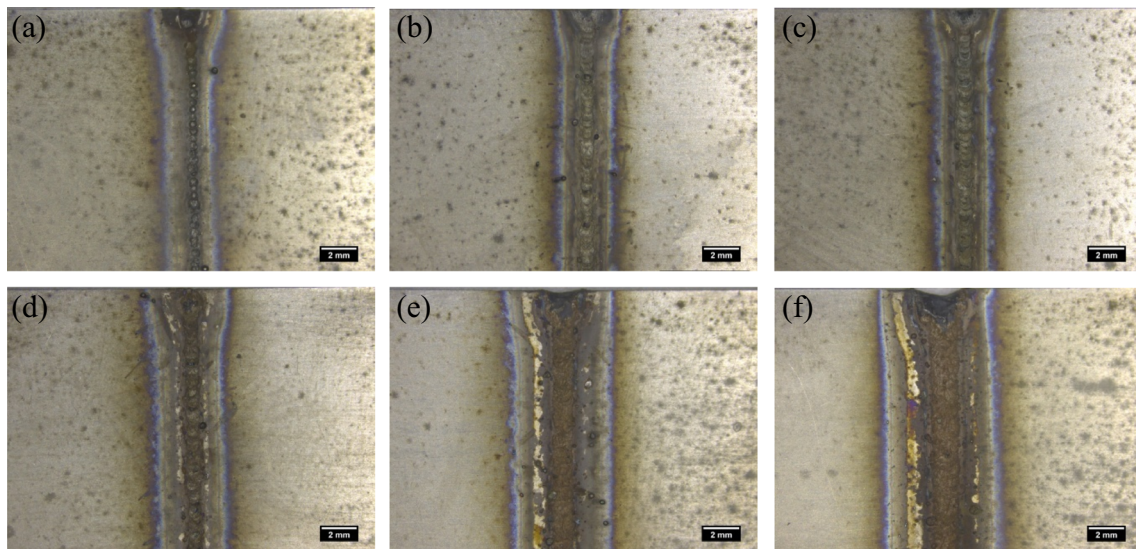
Fig. 5 Weld bead appearance of the root side/bottom surface of the welded joints at varying heat inputs: **a** 43.71 J/mm, **b** 48.57, **c** 49.98 J/mm, **d** 60 J/mm, **e** 75.6 J/mm, and **f** 103.5 J/mm

phase occurs during heating stage and changes into β-phase completely at 975 °C, and the β-phase remains stable up to 1605 °C (solidus temperature). The phase transformation takes place from α to β during heating stage and from β to α/α′ during cooling stage in the HAZ and fusion zone of the welded joint depending upon the cooling rate [34]. The change in heat input affects the microstructural phase change in the fusion zone and HAZ during LBW due to change in

Fig. 6 Optical microstructure of the weld bead shape at **a** 43.71 J/mm, **b** 48.57, **c** 49.98 J/mm, **d** 60 J/mm, **e** 75.6 J/mm, and **f** 103.5 J/mm
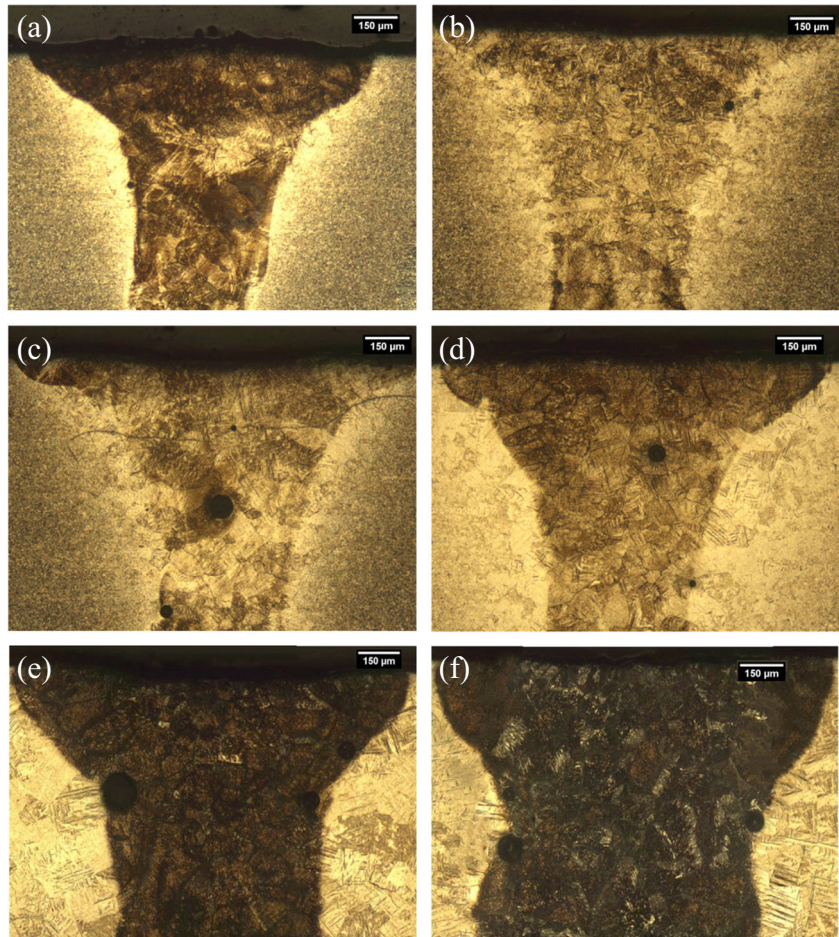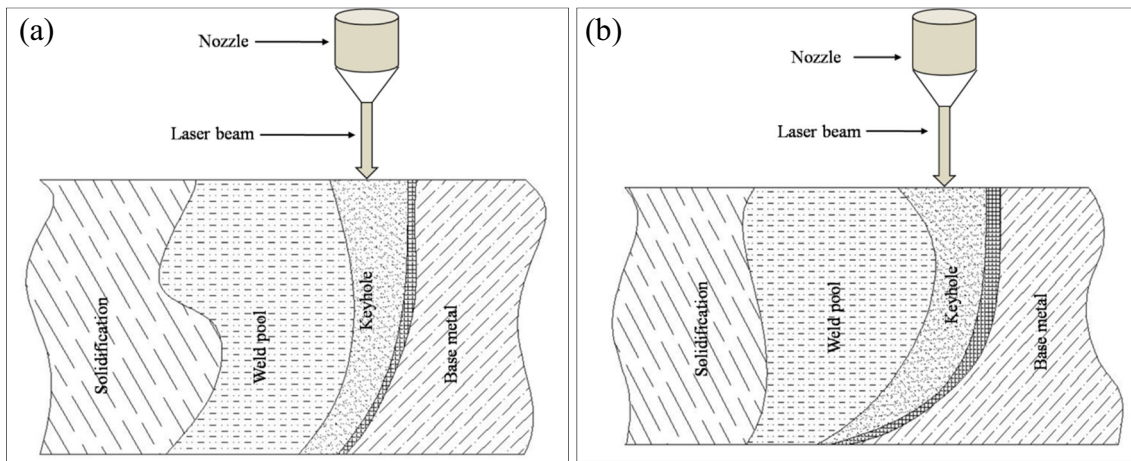
Fig. 7 Schematic diagram of the types of keyhole modes of penetration. **a** Open keyhole mode of penetration. **b** Closed keyhole mode of penetration

cooling rate. The cooling rate becomes faster at low heat input and it becomes slower at high heat input, and microstructural features change accordingly. At high heat input, the temperature of the weld zone and base metal increases, and therefore, the difference in thermal gradient between the weld zone and base metal nearby decreases which results decrease in cooling rate and vice versa occurs at low heat input. The change in

cooling rate promotes the microstructural phase change in the fusion zone and HAZ. Figure 11 shows the optical microstructure images of the fusion zone at varying heat inputs (43.71–103.5 J/mm), taken at magnification × 50. It is observed that large portion of β-phase is transformed into martensite (α′), blocky (α), and massive (α), when molten weld pool quenches at different heat inputs. It is observed that at low

Fig. 8 Influence of heat input on **a** fusion zone area, **b** fusion zone width (FZ top, FZ mid, and FZ bottom), and **c** HAZ width (HAZ top, HAZ mid, and HAZ bottom)
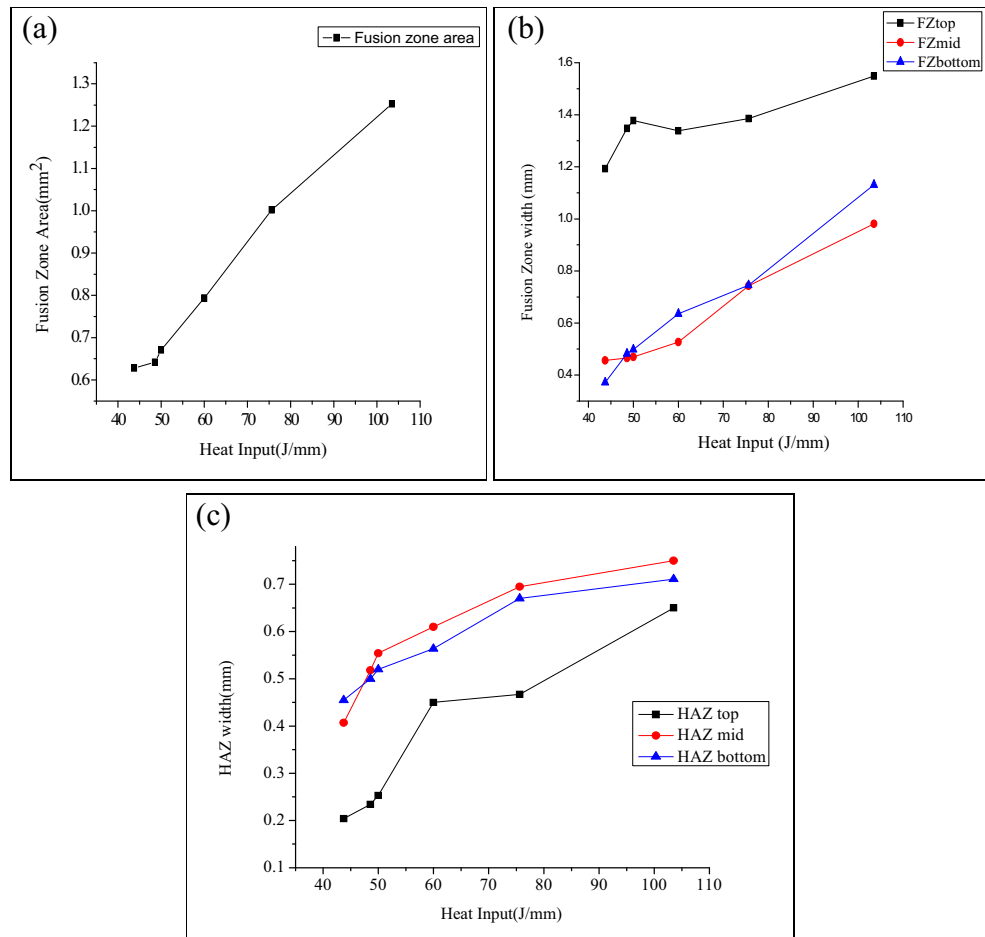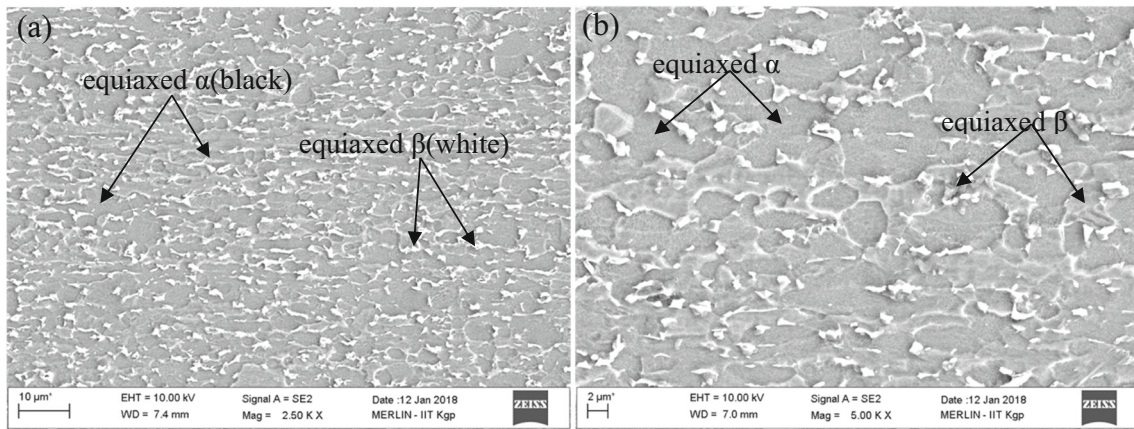
Fig. 9 Microstructure of the base metal. **a** FESEM image at × 2500 magnification. **b** FESEM image at × 5000 magnification

heat input (43.71, 48.57, 49.98 and 60 J/mm), the presence of martensitic α′ and α grain boundary has been found as shown in Fig. 11a–d. At low heat input, the cooling rate is high which promotes the formation of martensitic α′ in bulk amount. The presence of transformed martensite α′, massive α, and α grain boundary has been found at high heat input (75.6 and 103.5 J/mm) as shown in Fig. 11e, f because the cooling rate decreases with increase in heat input which promotes the formation of massive α.

Figure 12a–c shows the FESEM images of fusion zone for heat input of 43.71, 75.6, and 103.5 J/mm respectively at magnification of × 1000. It has been observed that α grain boundary size in the FZ increases with increase in heat input. The size of the α grain boundary in the FZ at heat input of 43.71 J/mm is smaller compared to that obtained at heat input of 75.6 and 103.5 J/mm because with increase in heat input, the energy supplied increases and cooling rate decreases which recrystallizes the grains forming coarse grains, as shown in Fig. 12a–c. The presence of massive α, formed due to transformation of α′, can be clearly seen at high heat input of 103.5 J/mm as shown in Fig. 12d (FESEM image at magnification × 2500). Martensitic α′ are needle shaped which are also visible from Fig. 12d.

Figure 13a–c shows the optical microstructure images of HAZ for exp. no. 6 (heat input = 103.5 J/mm) at various locations, namely, HAZ near fusion zone, middle of HAZ, and HAZ near the base metal, respectively. Different temperature gradients are imposed in HAZ region starting from HAZ near fusion zone to HAZ near BM during laser welding which results change in microstructural features in HAZ region. During laser welding, faster cooling rate and high peak temperature regions near HAZ are favorable for the phase transformation of α to β and β to α′ which results in disappearance of prior α-phase and formation of bulk amount of martensite α′. In the region far away from HAZ, i.e., near the base metal, partial transformation of α to other phases takes place because this region near to base metal is exposed to low temperature comparatively. Martensitic α′ and blocky α have been observed in the HAZ regions adjacent to FZ and middle of the HAZ as shown in Fig. 13a, b respectively. Blocky α, original β grains, and few martensitic α′ have been observed in the HAZ region adjacent to base metal as shown in Fig. 13c whereas equiaxed α and intergranular β grains have been observed in the parent metal as shown in Fig. 13d.

Figure 14 shows the FESEM images at × 2500 magnification, showing microstructures of HAZ at various heat inputs
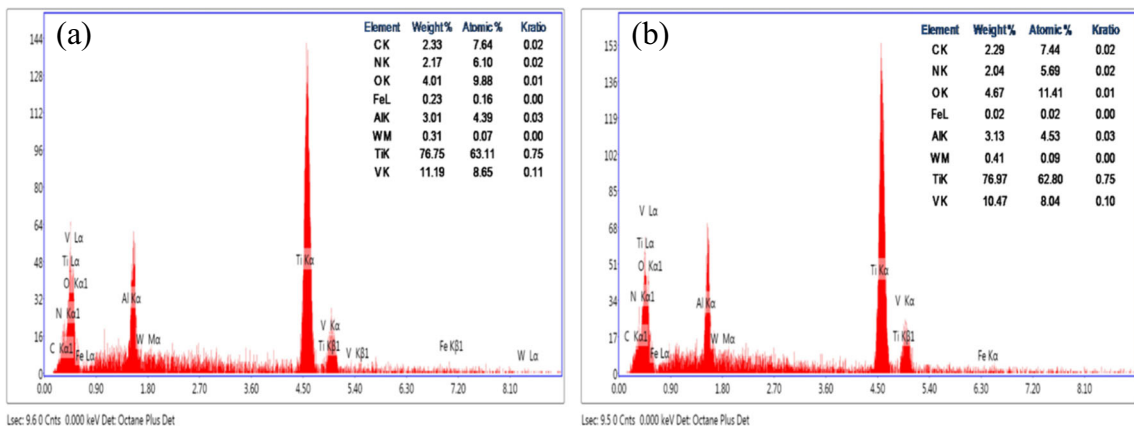

Fig. 10 EDS results of Ti6Al4V. **a** Base metal. **b** Fusion zone

Fig. 11 Optical microstructure of fusion zone at varying heat inputs: **a** exp. no. 1, heat input = 43.714 J/mm; **b** exp. no. 2, heat input = 48.57 J/mm; **c** exp. no. 3, heat input = 49.98 J/mm; **d** exp. no. 4, heat input = 60 J/mm; **e** exp. no. 5, heat input = 75.60 J/mm; **f** exp. no. 6, heat input = 103.5 J/mm
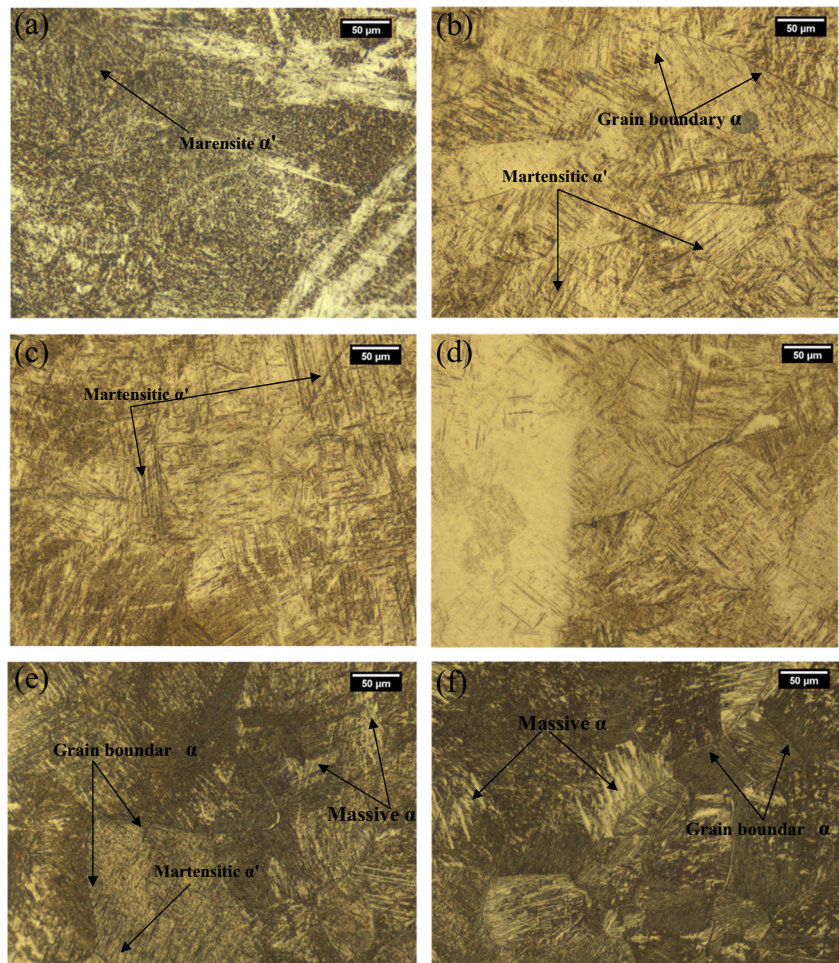

Fig. 12 FESEM images, showing microstructures of fusion zone for varying heat inputs: **a** heat input = 43.714 J/mm; **b** heat input = 75.6 J/mm; **c** heat input = 103.5 J/mm; **d** heat input = 103.5 J/mm at higher magnification
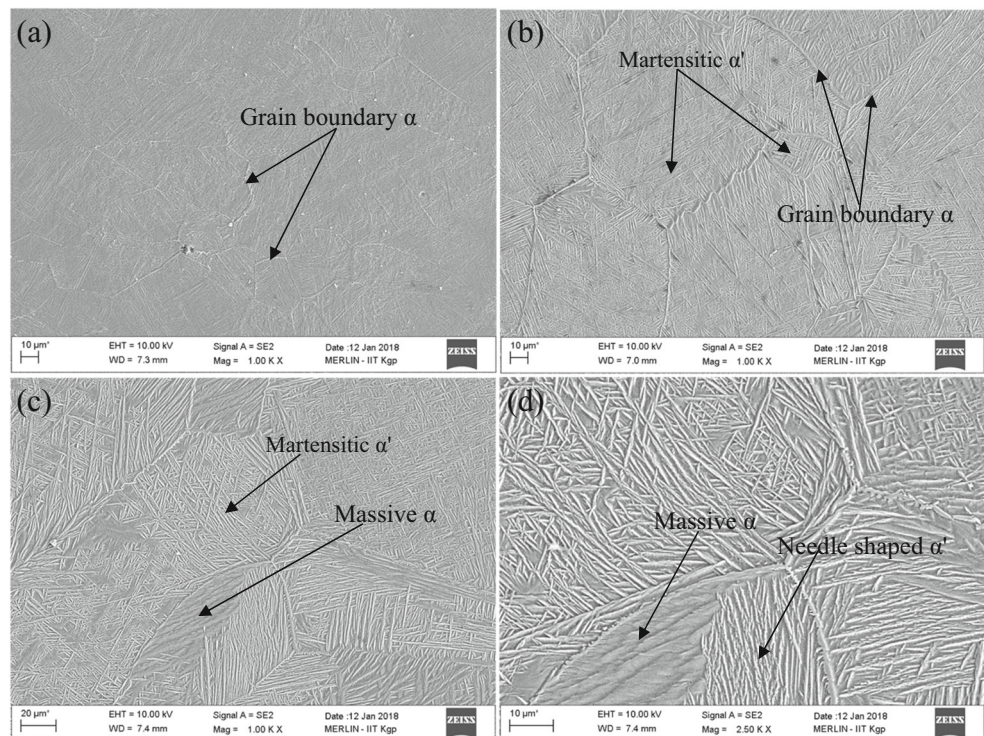
Fig. 13 Optical microstructure images for exp. no. 6. **a** HAZ near fusion zone. **b** Middle of HAZ. **c** HAZ near BM. **d** BM
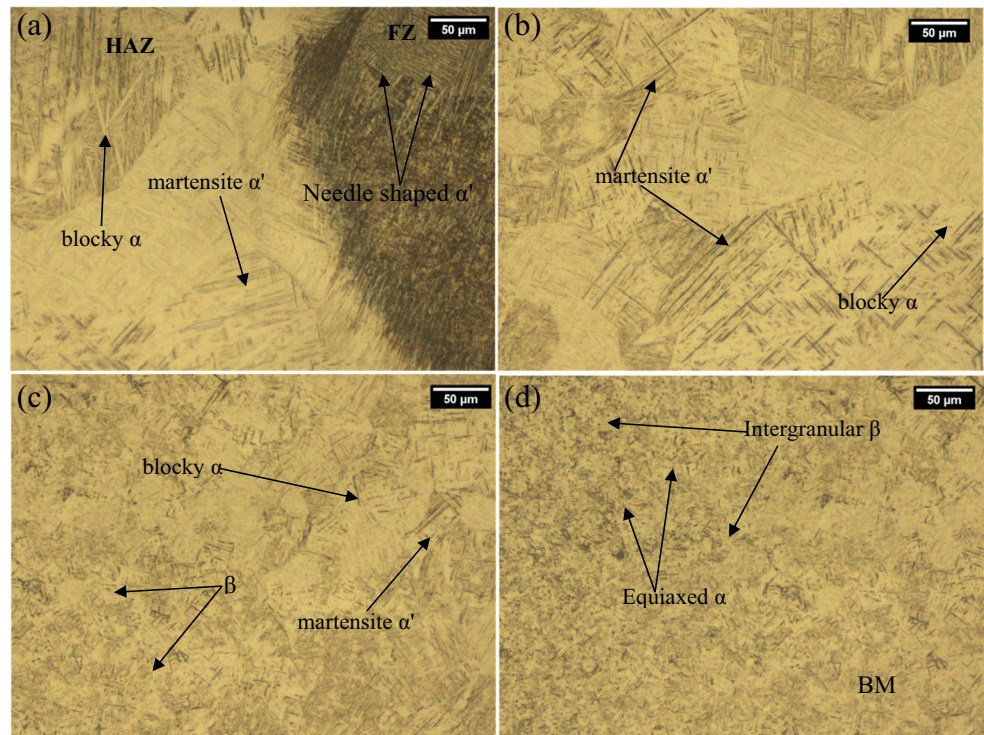
(43.71, 75.6, and 103.5 J/mm). Equiaxed α, granular β, and martensitic α' are observed at low heat input of 43.71 J/mm whereas needle-shaped (acicular α') prior β grains are seen at high heat input of 75.6 J/mm as shown in Fig. 14a, b respectively because of the difference of the cooling rate at low and

high heat input. Figure 14c shows the coarser acicular α' grains in the HAZ region comparatively.

The microstructural characterization of the laser-welded joints has also been done using high-resolution transmission electron microscope (TEM: model JEM-2100F). The TEM

Fig. 14 FESEM images at × 2500 magnification, showing microstructures of HAZ at varying heat inputs: **a** heat input = 43.714 J/mm; **b** heat input = 75.6 J/mm; **c** heat input = 103.5 J/mm
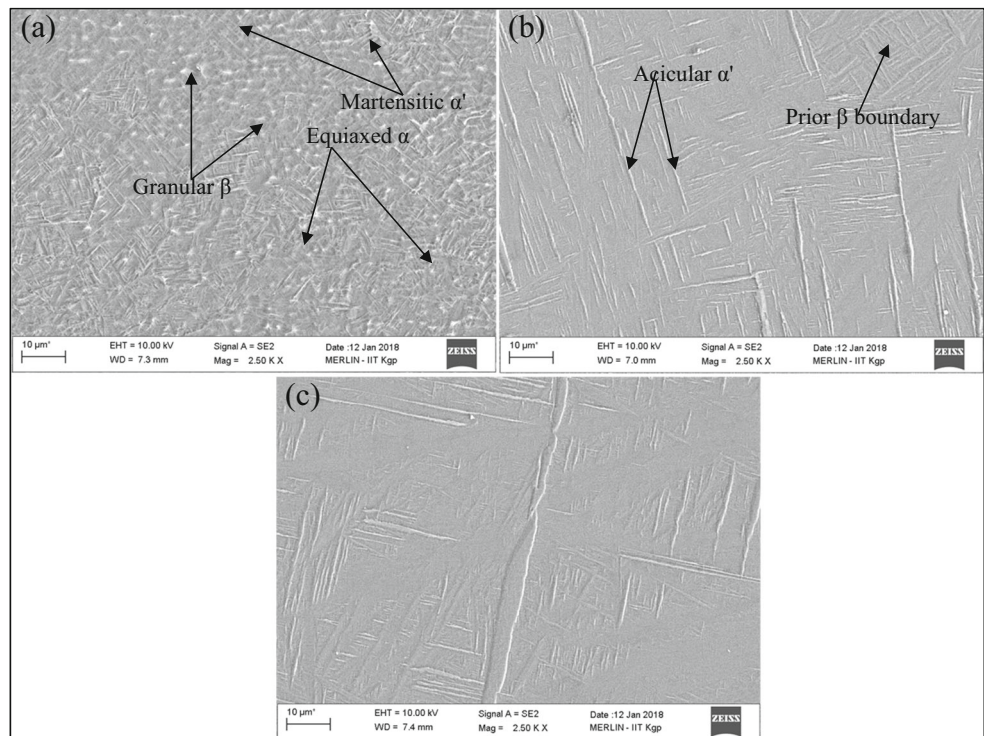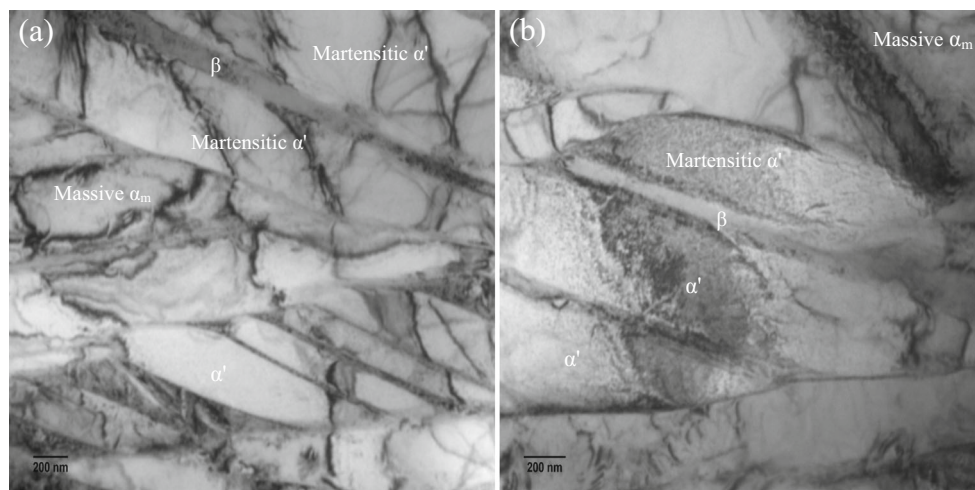
Fig. 15 TEM images of the fusion zone showing lamellar structure at **a** heat input = 49.98 J/mm and **b** heat input = 103.5 J/mm

parameters considered for the current study are as follows: 200 kV voltage, 95 μA dark current, 131 μA emission current, and 105.3 pA/cm^2 current density. For preparing TEM samples, firstly, 0.25-mm-thick specimens were extracted from the cross section of the welded joints. Then, the specimens were ground to 20-μm wafers and 3-mm-diameter circular TEM samples were punched from the cross sections and further ion milling was done using precision ion polishing system. The presence of lamellar structures has been found in the fusion zone of the laser-welded specimens as shown in Fig. 15. The parallel arrangement of acicular martensite α′ grains and β grains was observed in the fusion zone as shown in Fig. 15a, b at heat input of 49.98 and 103.5 J/mm, respectively. The β grains were sandwiched between the martensite

α′ grains. Coarser α′ grains were observed at high heat input of 103.5 J/mm compared to α′ grains at low heat input of 49.98 J/mm as shown in Fig. 15a, b.

3.5 Influence of heat input on pore formation in laser welds of Ti6Al4V

The formation of pores is a severe weld defect, during laser welding of Ti6Al4V as it degrades the mechanical properties of welded joints. Fusion welding of titanium alloys is prone to pore formation as reported by Huang et al. [35]. There are many possible reasons for the formation of pores during laser welding such as atmospheric gas entrapment, hydrogen gas emission, unstable keyhole, and vaporization of alloying

Fig. 16 FESEM microstructure images showing micropores at varying heat inputs: **a** heat input = 43.71 J/mm, **b** heat input = 49.98 J/mm, and **c** heat input = 75.6 J/mm
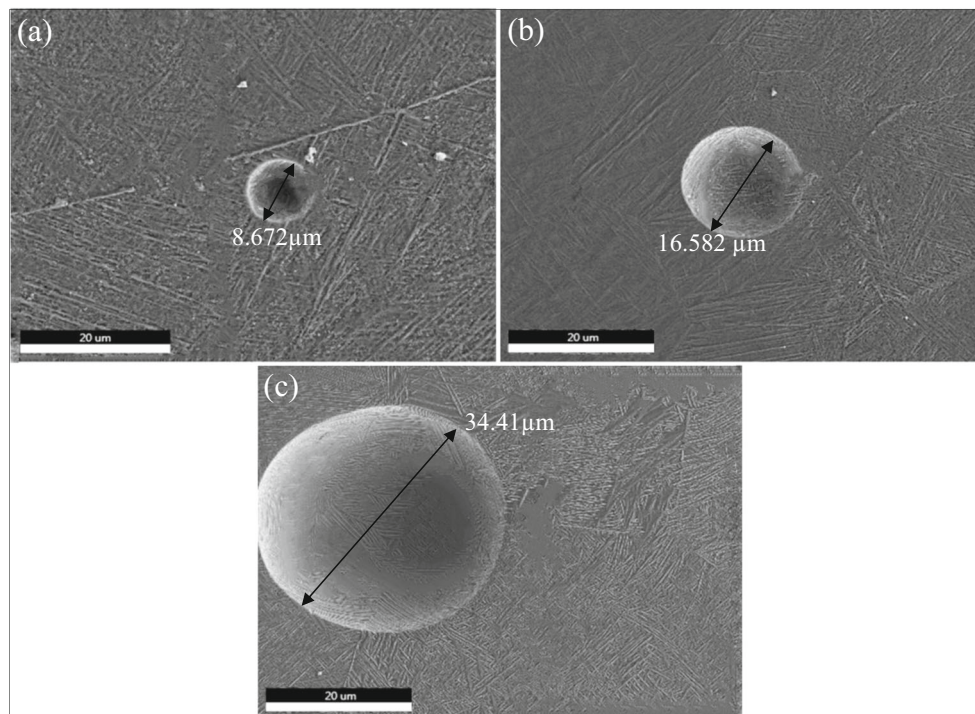
Fig. 17 Microhardness
distribution profile along the
transverse section of the laser-
welded joints for various heat
inputs: **a** 43.71 J/mm, **b** 48.57 J/
mm, **c** 49.98 J/mm, **d** 60 J/mm, **e**
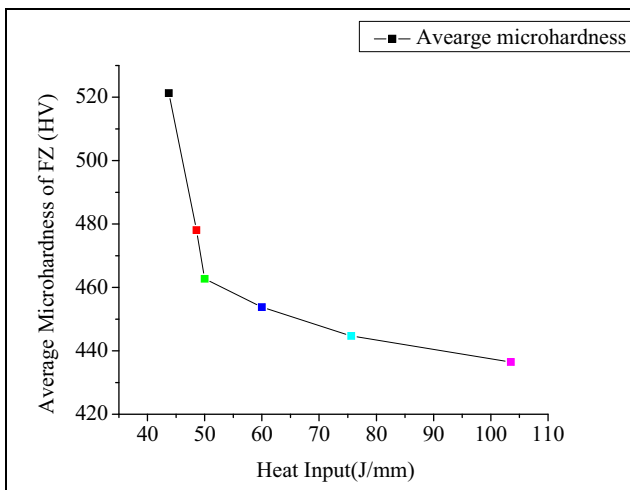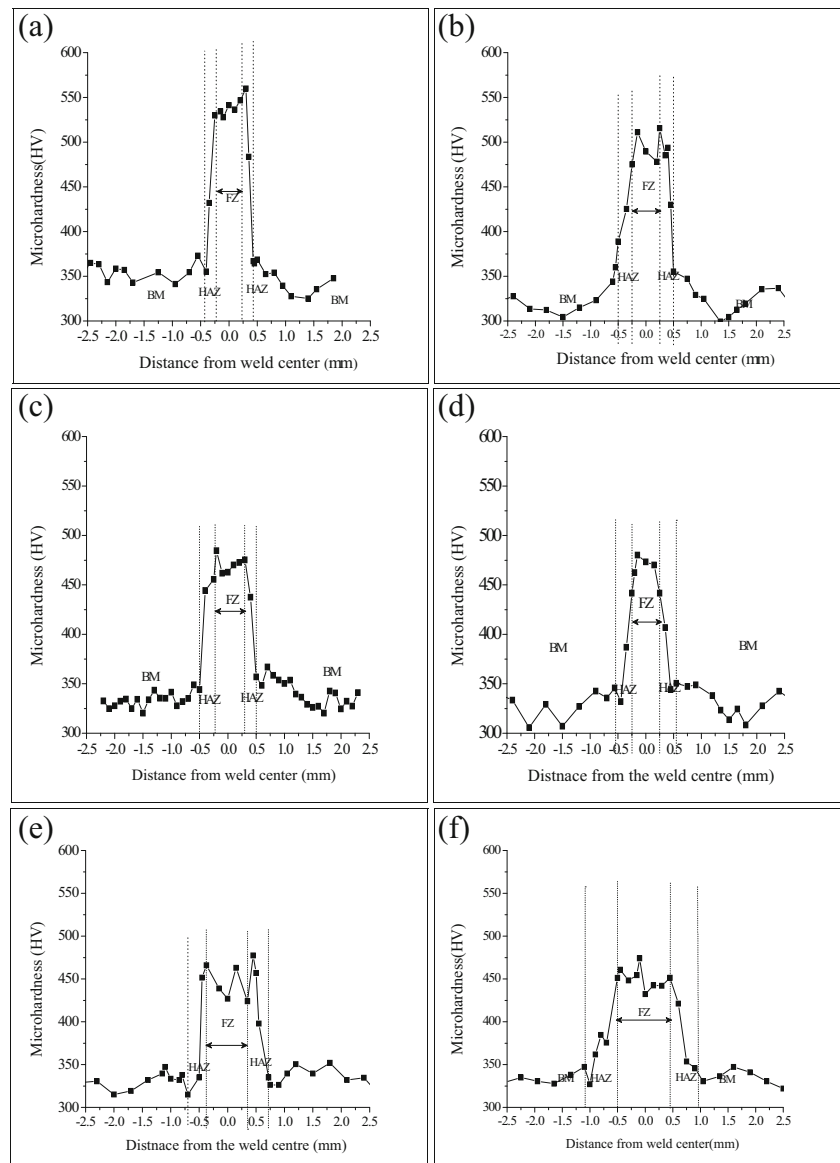75.6 J/mm, and **f** 103 J/mm

Fig. 18 Average microhardness of fusion zone as a function of heat input

elements having lower boiling point temperature. Figure 16
shows FESEM microstructure images showing micropores
present in fusion zone at heat input of 43.71, 49.98, and
75.6 J/mm (exp. 1, 3, and 5). It has been observed that at
low heat input (48.57, 49.98, and 60 J/mm), the micropores
are present at the upper portion of the fusion zone as shown in
Fig. 6b–d whereas at high heat input, the micropores are pres-
ent in the middle portion of the fusion zone adjacent to HAZ
region as shown in Fig. 6e, f. The size of the micropores also
increases with increase in heat input. The dimensions of the
micropores are 8.672, 16.582, and 34.41 μm at heat input of
43.714, 49.98, and 75.6 J/mm, respectively. As per the quality
acceptance criteria given by European BS EN:4678, micro-
pore diameter should be in the range of 6.28–46.44 μm [36].

Fig. 19 **a** Tensile specimen before the test and **b** tensile specimen after the test
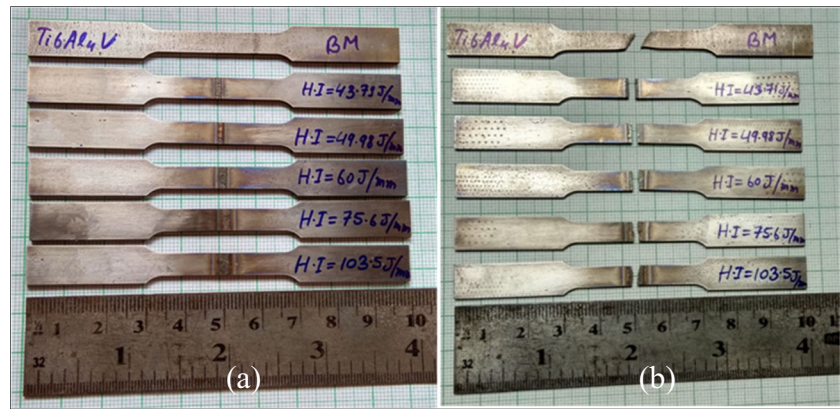
3.6 Influence of heat input on mechanical properties in the laser welds of Ti6Al4V

The influence of heat input on mechanical properties of Ti6Al4V laser-welded specimens have been studied in this section. Figure 17 shows the microhardness distribution along the transverse section of the laser-welded joints at varying heat inputs (43.71–103.5 J/mm), measured at the middle portion of the weld cross section. Vickers microhardness of the laser-welded joint was carried out at 0.98 N load with dwell time of 20 s on INNOVA TEST FALCON 500. The microhardness of the FZ is more than that of the HAZ and base metal due to the formation of acicular martensite α' in the FZ. The microhardness of the parent metal was nearly 335 HV, and for the FZ, it varies in the range of 436–521 HV. The average microhardness of fusion zone decreases with increase in heat input as shown in Fig. 18. The average microhardness value decreases with increase in heat input because the acicular α' and prior β grains present in the fusion zone become coarser with increase in heat input, which was clearly observed from the FESEM images shown in Fig. 12a–c. It has been observed

that at low heat input, the microhardness distribution across the HAZ decreases sharply from fusion zone and HAZ interface to base metal zone and HAZ interface where as high heat input microhardness does not decrease sharply because the original α- and β-phase of the base metal gets transformed to acicular α' phase, which increases the microhardness of HAZ equivalent to fusion zone and also increases the width of HAZ as shown in Fig. 17a–e.

Tensile test was done to analyze the ultimate tensile strength (UTS) and percentage elongation of base metal Ti6Al4V and laser-welded specimen. Figure 19a shows the base metal and welded tensile specimens before fracture, prepared as per ASTM E8 standards. The tensile specimens fractured from the weld zone after tensile test as shown in Fig. 19b. Stress-strain curve of the base metal and the welded joints at heat input of 49.98, 60, and 75.6 J/mm is shown in Fig. 20. It has been observed that the tensile strength of the laser-welded specimens is less than the parent metal due to the formation of pores in the fusion zone. The stress concentration increases at pore location during tensile loading and crack propagation starts from the micropores. The formation of fine
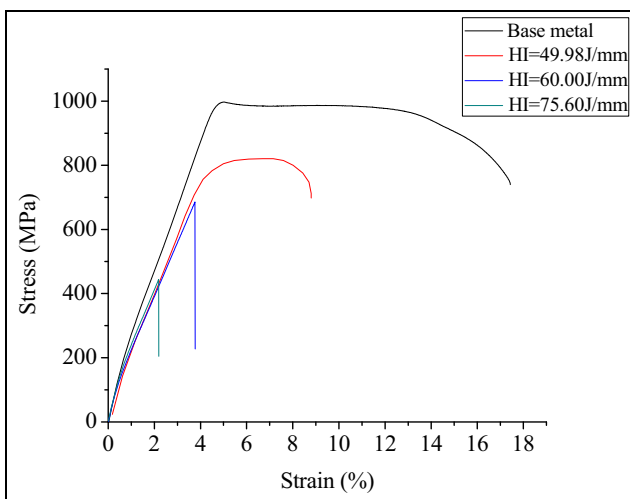

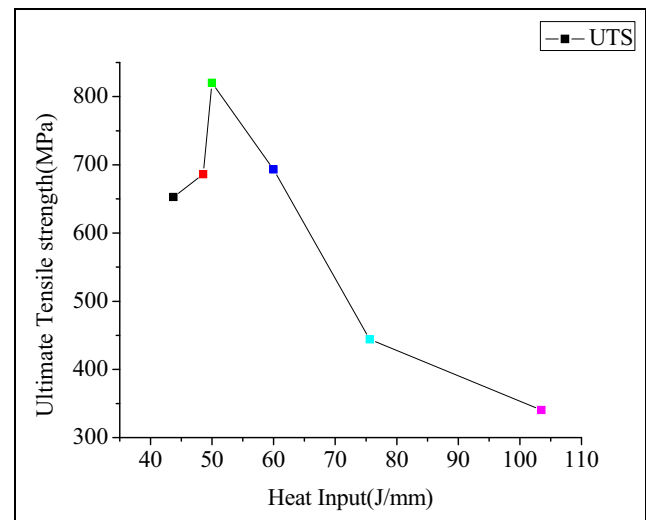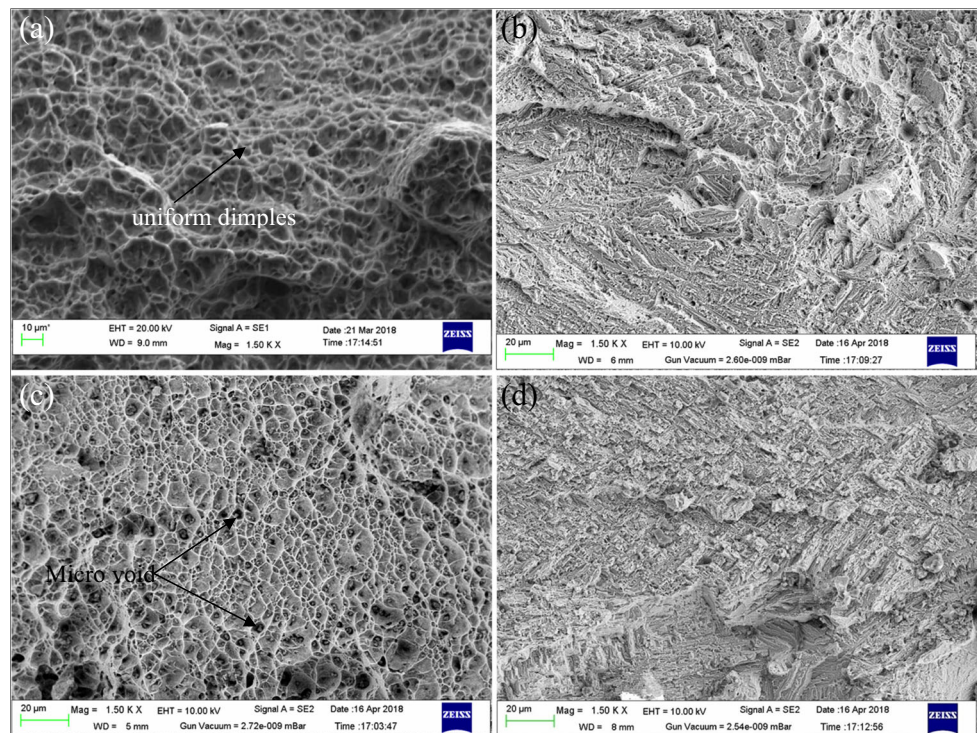**Fig. 20** Stress-strain curve of the base metal and the welded joints

Fig. 21 Effect of heat input on ultimate tensile strength

Fig. 22 FESEM images of fractured surface at × 1500 magnification of **a** base metal, **b** exp. no. 1 heat input = 43.71, **c** exp. no. 3 heat input = 49.98 J/mm, and **d** 75.6 J/mm

acicular martensite α' in the weld bead during LBW decreases the ductility of the welded joint. It has been observed that the UTS firstly increases with increase in heat input and becomes maximum and thereafter decreases as shown in Fig. 21. It has been also reported in the literature by Gao et al. [17] that the ductility of the laser-welded joints decreases with increase in overlapping factor (O_f) and the fracture behavior changes from ductile to quasi-cleavage manner (tending towards brittle nature).

Figure 22 shows FESEM images of tensile fractured surface at × 1500 magnification for base metal and welded joints at various heat input values (43.71, 49.98, and 75.6 J/mm). The fracture surface contains uniform and fine dimples with necking tip in the base metal Ti6Al4V as shown in Fig. 22a indicating the ductile fracture behavior. Brittle fracture surface

was observed in the welded joint performed at low heat input (43.71 J/mm) and high heat input (73.5 J/mm) as shown in Fig. 22b, d because at very low heat input (43.71), energy supplied is not sufficient whereas at very high heat input (73.5–103.5 J/mm), the pore size increases which increases the stress concentration and decreases the ductility as well as strength. Figure 22c shows the ductile fracture surface of the welded specimen at heat input of 49.98 J/mm with the presence of uniform dimples, and few microvoids were also present in the fracture surface. The ductile fracture of the welded specimen at heat input of 49.98 J/mm has also been observed from stress-strain curve shown in Fig. 20. UTS of the welded joint for exp. no. 3 is less than the parent base metal due to the presence of microvoids. The fracture of the welded joint is brittle at high heat input due to the presence of large size of

Fig. 23 Showing **a** ultimate tensile strength (UTS) and **b** elongation (%) for base metals and laser welded at various heat inputs
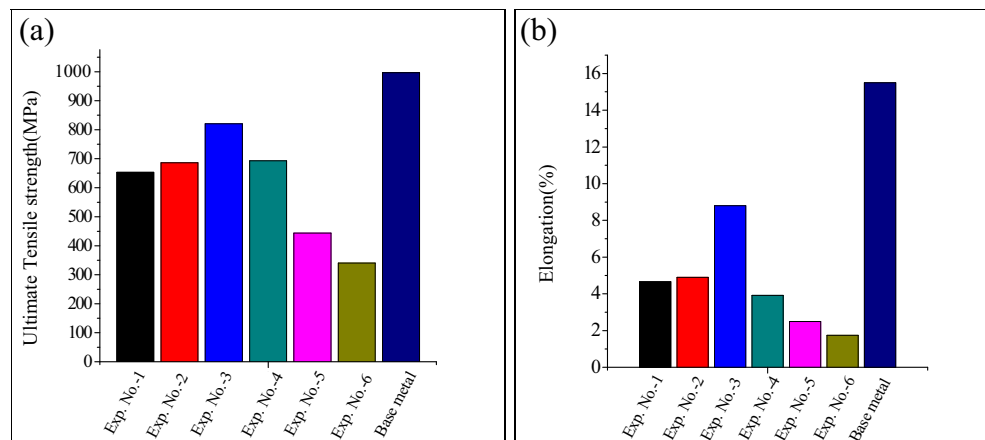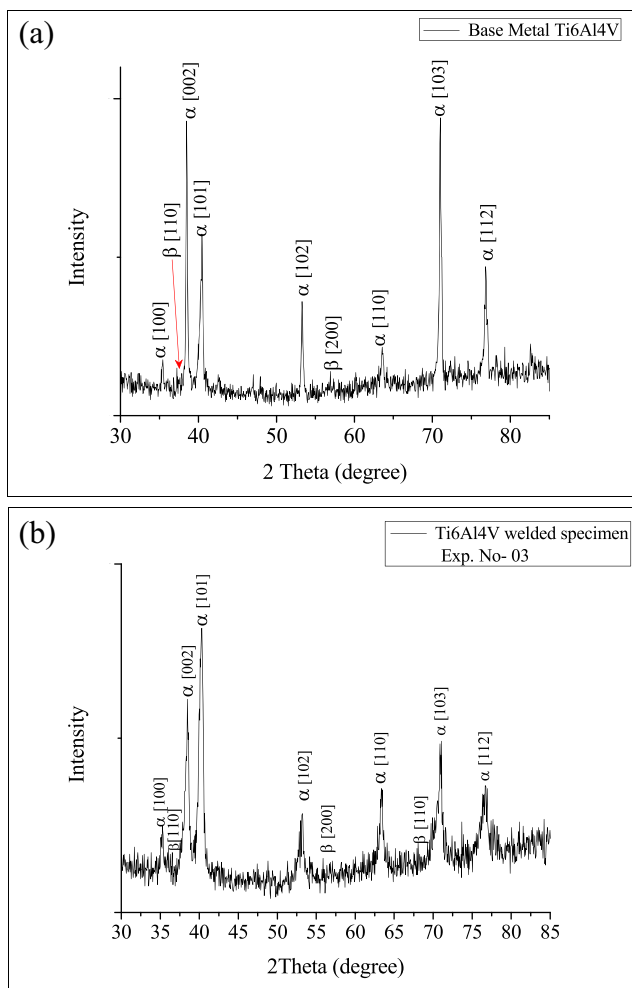
Fig. 24 XRD spectrum pattern peaks for **a** base metal Ti6Al4V and **b** welded zone for exp. no. 3

micropores and coarser prior β grains in the fusion zone which increases the stress concentration. Figure 23a, b shows the UTS and elongation (%) of the parent metal and welded joints. The tensile strength and elongation (%) for exp. no. 3 are maximum compared to all the welded joints but less than the parent metal due to the presence of small-sized micropores.

3.7 XRD analysis

X-ray diffraction (XRD) investigation of the base metal Ti6Al4V and welded sample for exp. no. 3 has been performed in this section to study the crystallographic structure at various positions (2θ°). The XRD pattern peaks of the as-received base metal Ti6Al4V and welded specimen are shown in Fig. 24a, b, respectively, measured in the range of 30 to 85°. As shown in Fig. 24a, XRD spectrum pattern peaks for base metal Ti6Al4V show the presence of α-phase characterized by hkl values containing (100), (002), (101), (102), (110), (103), and (112) reflections matched with reference data available.

Base metal Ti6Al4V also contains β-phase characterized by hkl values containing (110) and (200). XRD spectrum pattern contains both α-phase (hcp) and β-phase (bcc) at heat input of 49.98 J/mm in the welded specimen. It has been observed that the XRD pattern peaks of the weld zone are dominated by α-phase (hcp) spectrum peaks and few bcc spectrum peaks because the transformation of α-β-phase occurs during heating process in laser welding.

4 Conclusion

In the present investigation, pulsed Nd:YAG laser welding of titanium alloy (Ti6Al4V) of 1.4 mm thickness has been carried out at different laser process parameters in butt joint configuration. The influence of heat input on weld surface morphology, weld bead shape, FZ width, HAZ width, FZ area, microstructure, and mechanical properties has been studied. Based on the experimental work performed, the following observation can be concluded:

- The shape of the weld bead profile is T-shaped at low heat input (43.71, 48.57, 49.98, 60, and 75.6 J/mm) and becomes approximately X-shaped at high heat input (103.5 J/mm).
- Fusion zone area, fusion zone width, and HAZ width increase with increase in heat input.
- The average microhardness of the fusion zone decreases with increase in heat input, and the microhardness of the fusion zone is greater than that of the HAZ and base metal due to the formation of α′ martensite in the fusion zone.
- Tensile strength firstly increases with increase in heat input and attains maximum value of 820.67 MPa at heat input of 49.98 J/mm and decreases further with increase in heat input beyond 49.98 J/mm as micropore size increases with increase in heat input which results high stress concentration in the FZ.
- At low heat input (43.71, 48.57, 49.98, and 60 J/mm), the presence of martensitic α′ and α grain boundary has been observed whereas at high heat input (75.6 and 103.5 J/mm), the presence of transformed martensite α′, massive α, and α grain boundary has been found due to the difference in cooling rate at low and high heat input.
- The size of the micropores also increases with increase in heat input. The dimensions of the micropores present in the FZ are 8.672, 16.582, and 34.41 μm at heat input of 43.714, 49.98, and 75.6 J/mm, respectively.

References

1. Li Z, Gobbi SL, Norris I, Zolotovsky S, Richter KH (1997) Laser welding techniques for titanium alloy sheet. J Mater Process Technol 65:203–208
2. Elias CN, Lima JHC, Valiev R, Meyers MA (2008) Biomedical applications of titanium and its alloys. JOM 60:46–49
3. Balasubramanian TS, Balasubramanian V, Manickam MM (2011) Fatigue crack growth behaviour of gas tungsten arc, electron beam and laser beam welded Ti–6Al–4V alloy. Mater Des 32:4509–4520
4. Chen YC, Nakata K (2009) Microstructural characterization and mechanical properties in friction stir welding of aluminum and titanium dissimilar alloys. Mater Des 30:469–474
5. Yunlian Q, Ju D, Quan H, Liying Z (2000) Electron beam welding, laser beam welding and gas tungsten arc welding of titanium sheet. Mater Sci Eng A 280:177–181
6. Lima MSFD (2005) Laser beam welding of titanium nitride coated titanium using pulse-shaping. Mater Res 8:323–328
7. Bertrand C, Laplanche O, Rocca JP, Le Petitcorps Y, Nammour S (2007) Effect of the combination of different welding parameters on melting characteristics of grade 1 titanium with a pulsed Nd–Yag laser. Lasers Med Sci 22:237–244
8. Costa A, Miranda R, Quintino L, Yapp D (2007) Analysis of beam material interaction in welding of titanium with fiber lasers. Mater Manuf Process 22:798–803
9. Liu J, Watanabe I, Yoshida K, Atsuta M (2002) Joint strength of laser-welded titanium. Dent Mater 18:143–148
10. Colegrove P, Simiand PE, Varughese A, Williams S, Yapp D (2009) Evaluation of a drilling model approach to represent laser spot microwelding. In Trends in welding research, ASM Proceedings of the 8th International Conference 2008, pp. 303–312
11. Torkamany MJ, Hamedi MJ, Malek F, Sabbaghzadeh J (2006) The effect of process parameters on keyhole welding with a 400 W Nd: YAG pulsed laser. J Phys D Appl Phys 39(21):4563–4567
12. Chen Y, Chen S, Li L (2009) Effects of heat input on microstructure and mechanical property of Al/Ti joints by rectangular spot laser welding-brazing method. Int J Adv Manuf Technol 44(3–4):265–272
13. Torkamany MJ, Ghaini FM, Papan E, Dadras S (2012) Process optimization in titanium welding with pulsed Nd: YAG laser. Sci Adv Mater 4:489–496
14. Akman E, Demir A, Canel T, Sınmazçelik T (2009) Laser welding of Ti6Al4V titanium alloys. J Mater Process Technol 209:3705–3713
15. Gao XL, Zhang LJ, Liu J, Zhang JX (2014) Effects of weld cross-section profiles and microstructure on properties of pulsed Nd: YAG laser welding of Ti6Al4V sheet. Int J Adv Manuf Technol 72:895–903
16. Xu PQ (2012) Microstructure characterization of Ti–6Al–4V titanium laser weld and its deformation. Trans Nonferrous Metals Soc China 22:2118–2123
17. Gao XL, Liu J, Zhang LJ, Zhang JX (2014) Effect of the overlapping factor on the microstructure and mechanical properties of pulsed Nd: YAG laser welded Ti6Al4V sheets. Mater Charact 93:136–149
18. Gursel A (2017) Crack risk in Nd: YAG laser welding of Ti-6Al-4V alloy. Mater Lett 197:233–235
19. Caiazzo F, Alfieri V, Astarita A, Squillace A, Barbieri G (2016) Investigation on laser welding of Ti-6Al-4V plates in corner joint. Adv in Mech Eng 9:1687814016685546
20. Kumar C, Das M, Paul CP, Singh B (2017) Experimental investigation and metallographic characterization of fiber laser beam welding of Ti-6Al-4V alloy using response surface method. Opt Lasers Eng 95:52–68
21. Campanelli SL, Casalino G, Mortello M, Angelastro A, Ludovico AD (2015) Microstructural characteristics and mechanical properties of Ti6Al4V alloy fiber laser welds. Procedia CIRP 33:428–433
22. Caiazzo F, Alfieri V, Corrado G, Cardaropoli F, Sergi V (2013) Investigation and optimization of laser welding of Ti-6Al-4 V titanium alloy plates. J Manuf Sci Eng 135:061012
23. Akbari M, Saedodin S, Toghraie D, Shoja-Razavi R, Kowsari F (2014) Experimental and numerical investigation of temperature distribution and melt pool geometry during pulsed laser welding of Ti6Al4V alloy. Opt Laser Technol 59:52–59
24. Oliveira JP, Miranda RM, Fernandes FB (2017) Welding and joining of NiTi shape memory alloys: a review. Prog Mater Sci 88:412–466
25. Oliveira JP, Panton B, Zeng Z, Andrei CM, Zhou Y, Miranda RM, Fernandes FB (2016) Laser joining of NiTi to Ti6Al4V using a niobium interlayer. Acta Mater 105:9–15
26. Auwal ST, Ramesh S, Yusof F, Manladan SM (2018) A review on laser beam welding of titanium alloys. Int J Adv Manuf Technol 97:1071–1098
27. Sjögren G, Andersson M, Bergman M (1988) Laser welding of titanium in dentistry. Acta Odontol Scand 46:247–253
28. Palanivel R, Dinaharan I, Laubscher RF (2017) Microstructure evolution and mechanical characterization of Nd: YAG laser beam welded titanium tubes. Mater Charact 134:225–235
29. Gao XL, Liu J, Zhang LJ (2018) Effect of heat input on microstructure and mechanical properties of pulsed laser welded joints in Ti6Al4V/Nb dissimilar alloys. Int J Adv Manuf Technol 94:3937–3947
30. Standard ASTM (2011) E3 Standard guide for preparation of metallographic specimens. West Conshohocken (PA): ASTM International
31. ASTM E8/E8M (2013) Standard test methods for tension testing of metallic materials. West Conshohocken (PA): ASTM International
32. Hong KM, Shin YC (2016) Analysis of microstructure and mechanical properties change in laser welding of Ti6Al4V with a multiphysics prediction model. J Mater Process Technol 237:420–429
33. Squillace A, Prisco U, Ciliberto S, Astarita A (2012) Effect of welding parameters on morphology and mechanical properties of Ti–6Al–4V laser beam welded butt joints. J Mater Process Technol 212:427–436
34. Elmer JW, Palmer TA, Babu SS, Zhang W, DebRoy T (2004) Phase transformation dynamics during welding of Ti–6Al–4V. J Appl Phys 95:8327–8339
35. Huang JL, Warnken N, Gebelin JC, Strangwood M, Reed RC (2012) On the mechanism of porosity formation during welding of titanium alloys. Acta Mater 60:3215–3225
36. EN BS (2011) 4678 Aerospace series. Weldments and brazements for aerospace structures. Joints of metallic materials by laser beam welding. Quality of weldments BSI